Optical properties and electronic correlations in $La_3Ni_2O_7$ bilayer nickelates under high pressure

Benjamin Geisler,[1,2,*] Laura Fanfarillo,[3] James J. Hamlin,[1] Gregory R. Stewart,[1] Richard G. Hennig,[2,4] and P.J. Hirschfeld[1]

[1]*Department of Physics, University of Florida, Gainesville, Florida 32611, USA*
[2]*Department of Materials Science and Engineering, University of Florida, Gainesville, Florida 32611, USA*
[3]*Istituto dei Sistemi Complessi (ISC-CNR), Via dei Taurini 19, I-00185 Rome, Italy*
[4]*Quantum Theory Project, University of Florida, Gainesville, Florida 32611, USA*

(Dated: November 4, 2024)

We explore the optical properties of $La_3Ni_2O_7$ bilayer nickelates by using density functional theory including a Coulomb repulsion term. Convincing agreement with recent experimental ambient-pressure spectra is achieved for $U \sim 3$ eV, which permits tracing the microscopic origin of the characteristic features. Simultaneous consistency with angle-resolved photoemission spectroscopy and x-ray diffraction suggests the notion of rather moderate electronic correlations in this novel high-T_c superconductor. Oxygen vacancies form predominantly at the inner apical sites and renormalize the optical spectrum quantitatively, while the released electrons are largely accommodated by a defect state. We show that the structural transition occurring under high pressure coincides with a significant enhancement of the Drude weight and a reduction of the out-of-plane interband contribution that act as a fingerprint of the emerging hole pocket. We further calculate the optical spectra for various possible magnetic phases including spin-density waves and discuss the results in the context of experiment. Finally, we investigate the role of the 2-2 versus 1-3 layer stacking and compare the bilayer nickelate to $La_4Ni_3O_{10}$, $La_3Ni_2O_6$, and $NdNiO_2$, unveiling general trends in the optical spectrum as a function of the formal Ni valence in Ruddlesden-Popper versus reduced Ruddlesden-Popper nickelates.

I. INTRODUCTION

The recent observation of superconductivity with $T_c \sim 80$ K in pressurized $La_3Ni_2O_7$ [1–3] suggested the bilayer Ruddlesden-Popper compounds as an intriguing new member of the steadily growing family of superconducting nickelates [4–10] and instantly sparked considerable interest [11–40]. Despite these efforts, several aspects remain unclear so far. Specifically, the pairing mechanism and its relation to the pressure-driven structural transition from a $Cmcm$ to an $Fmmm$ [1, 23, 29] or $I4/mmm$ space group [31, 37], both involving a suppression of the NiO_6 octahedral rotations, is still intensely debated [12–14, 22, 23, 28, 39].

The key ingredient to understand superconductivity on a fundamental level is an appropriate electronic structure. This necessitates a careful assessment of *ab initio* results and specifically raises a question about the role of electronic correlations in $La_3Ni_2O_7$. Angle-resolved photoemission spectroscopy (ARPES) reported a two-band Fermi surface at ambient pressure [34]. Simultaneously, the formation of an additional Ni-$3d_{z^2}$-derived flat band around the zone corner, $\sim$ 50 meV below the Fermi level, has been observed [34]. Density functional theory analysis of the Drude peak in the in-plane optical conductivity similar to Qazilbash *et al.* [41] suggested that $La_3Ni_2O_7$ features strong electronic correlations, placing it in terms of Mottness close to the reference superconductor La_2CuO_4 [30].

Intriguingly, optical spectra permit deeper insight into the electronic structure in a more complete energy window via the interband transitions. The availability of recently measured experimental data provides a unique opportunity to estimate the correlation effects by following this distinct route.

This motivated us to explore the optical properties of $La_3Ni_2O_7$ bilayer nickelates from first principles including a Coulomb repulsion term. Convincing agreement with the experimental spectrum at ambient pressure is achieved for $U \sim 3$ eV, which puts us in position to trace the microscopic origin of its characteristic features. In addition to the in-plane optical conductivity, we also predict the out-of-plane component, uncovering an unexpectedly strong anisotropy that reverses as a function of frequency. Simultaneously, Ni $3d_{z^2}$ energies consistent with recent ARPES results and accurate lattice parameters are obtained, establishing the notion of rather moderate electronic correlations in $La_3Ni_2O_7$. Moreover, we provide trends in the optical spectrum due to explicit oxygen vacancies, which predominantly occur at the inner apical sites. The released electrons are largely accommodated by an emergent defect state, in sharp contrast to doping the system.

Subsequently, we predict that the structural transition occurring under high pressure is accompanied by a significant enhancement of the Drude peak and a reduction of the out-of-plane interband contribution, which opens a route to track the proposed changes in Fermi surface topology [1, 11–14, 23, 28] in future c-axis measurements. The impact of different magnetic phases including spin-density waves is investigated. Finally, we uncover a distinct optical signature of the 2-2 versus 1-3 layer stacking [42, 43] and discuss the bilayer compound in the broader context of related Ruddlesden-Popper and reduced Ruddlesden-Popper nickelates, identifying fundamental differences between the two families, but also general trends in the optical response relating to the formal Ni valence.

* benjamin.geisler@ufl.edu

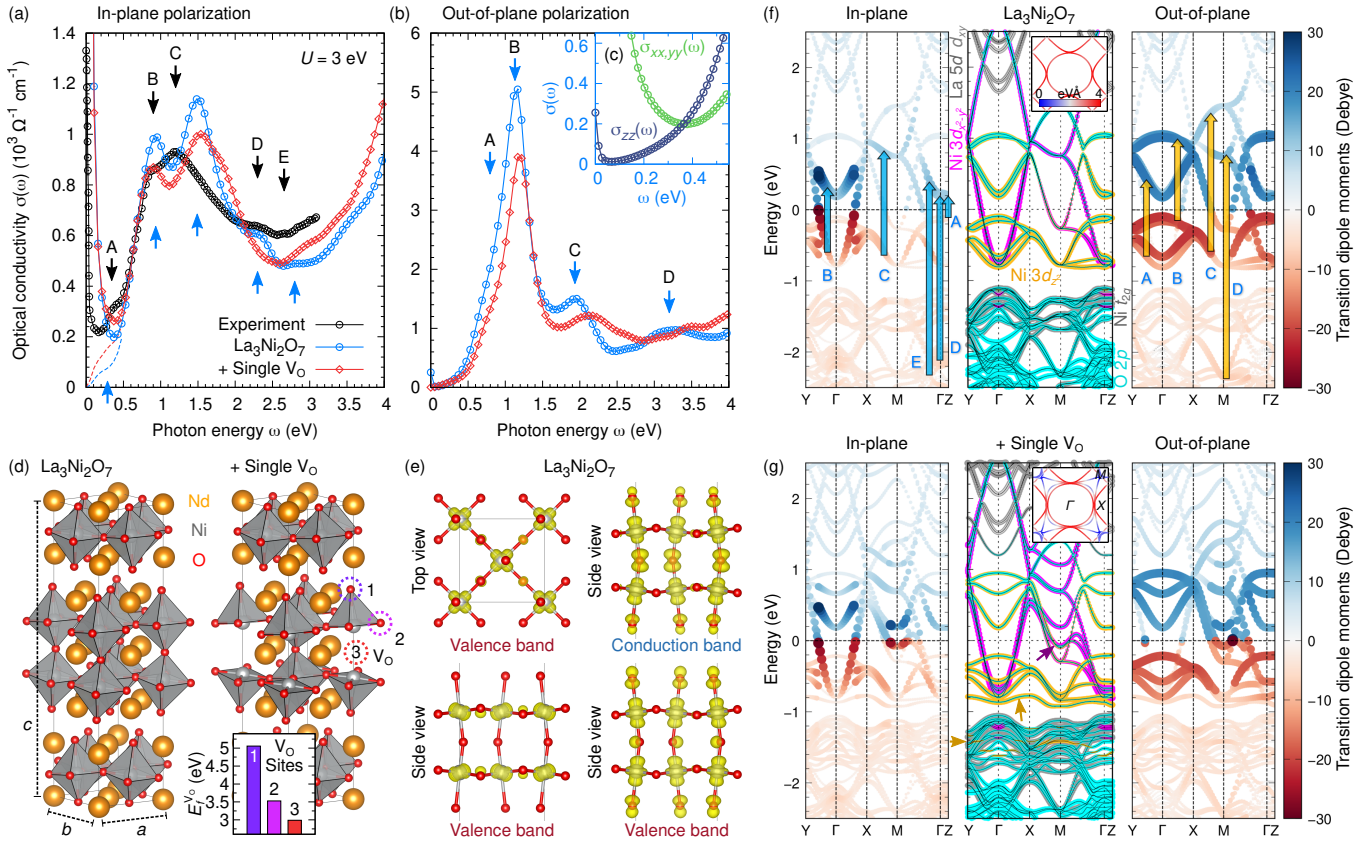

Figure 1. **Optical properties of $La_3Ni_2O_7$ at ambient pressure.** (a) Optical in-plane conductivity $\sigma_{xx,yy}(\omega)$ and (b) out-of-plane conductivity $\sigma_{zz}(\omega)$, comparing DFT+U results for the stoichiometric case (blue) and in the presence of an explicit oxygen vacancy (V_O) (red) to the experimental data (black [30]), which uncovers very good qualitative and quantitative agreement for the interband transitions. The dashed lines at low energies represent exclusively the interband contributions. (c) Low-energy anisotropy $\sigma_{xx,yy}(\omega)$ versus $\sigma_{zz}(\omega)$ of $La_3Ni_2O_7$ from panels (a,b). (d) Corresponding optimized geometries, together with the site-resolved V_O formation energies. (e) Selected Γ-point wave functions (absolute square) in $La_3Ni_2O_7$ of the occupied Ni $3d_{x^2-y^2}$ (top and side view), occupied 'bonding' Ni $3d_{z^2}$, and empty 'antibonding' Ni $3d_{z^2}$ states, revealing a distinct involvement of the inner apical oxygen ions. (f,g) Energy- and k-resolved transition dipole moments $|P^2_\alpha(n,\vec{k})|^{0.5}$ (initial and final states depicted in red and blue, respectively) together with the orbital-resolved band structure. Large arrows mark the characteristic transitions shown in panels (a,b). Small arrows highlight key differences in the band structure induced by the explicit V_O. The insets show the corresponding Fermi surfaces, colored by the Fermi velocity.

II. RESULTS

A. Optical spectrum, dipole transition analysis, and impact of oxygen vacancies

We begin with a detailed analysis of the in-plane optical conductivity $\sigma_{xx,yy}(\omega)$ of $La_3Ni_2O_7$ at ambient pressure [Fig. 1(a); $Cmcm$ space group] and close comparison with recently measured data obtained from reflectivity experiments [30]. At least four characteristic interband peaks can be identified in the experimental spectrum: A small prepeak at around $\omega \sim 0.35$ eV (A), two dominant peaks at 0.9 eV (B) and 1.2 eV (C), and a smaller peak at 2.3 eV (D). Interestingly, we find that the simulated spectrum obtained for $U = 3$ eV nicely reproduces these features both qualitatively and quantitatively. The quantitative agreement (i.e., the peak intensities and peak energies) is particularly good for peaks B and D, whereas the energy of peak C is overestimated by 0.3 eV. Furthermore, close inspection uncovers a small fifth peak at $\omega \sim 2.7$ eV (E) that is reproduced at ~ 2.8 eV. The simulation even predicts a finite spectral weight near peak A. Since the experimental in-plane Drude peak is significantly renormalized [30], as one can see by comparing to our simulated result, such low-energy interband features can be clearly resolved.

The convincing agreement of the simulated spectrum for $La_3Ni_2O_7$ and experimental observations puts us in a position to trace the microscopic origin of its characteristic features. The energy- and k-resolved TDMs $P^2_\alpha(n,\vec{k})$ in conjunction with the orbital-resolved band structure [Fig. 1(f)] allow us to identify spectral peaks B and C to in-plane polarized transitions between Ni $3d_{x^2-y^2}$ and Ni $3d_{z^2}$ states. The low-energy spectral weight (A) stems from excitations in the immediate vicinity of the Fermi level, particular at finite k_z,

which are promoted by the substantial octahedral rotations. At higher energies, transitions from the O $2p$ valence states to the Ni $3d_{z^2}$ states can be observed (D, E).

The predicted out-of-plane optical conductivity $\sigma_{zz}(\omega)$ [Fig. 1(b)], while smaller for low energies as expected in a layered system (see inset), exceeds the in-plane components substantially for $\omega > 0.35$ eV and uncovers a strong anisotropy of the optical response. The spectrum features a very pronounced peak at ~ 1.1 eV that consists of at least two distinct contributions (A, B), a smaller peak at ~ 1.9 eV (C), and a broad peak around 3.2 eV (D). The Drude peak is rather negligible. We attribute these features to strong transitions between the occupied 'bonding' Ni $3d_{z^2}$ states and empty 'antibonding' Ni $3d_{z^2}$ states (A, B) as well as unoccupied Ni $3d_{z^2}$–Ni $3d_{x^2-y^2}$–O $2p$ hybrid states around the M point (C), but also to excitations from the O $2p$ valence states to Ni $3d_{x^2-y^2}$ states (D) [Fig. 1(f)]. Interestingly, comparison of the TDMs thus reveals that light with varying polarization excites transitions between highly distinct electronic states in these novel nickelate compounds.

Figure 1(e) visualizes the Γ-point wave functions of selected states in $La_3Ni_2O_7$ that contribute prominently to the optical spectrum. We see that the states extend over the entire bilayer due to the substantial Ni $3d$-O $2p$ hybridization. In the Ni-$3d_{x^2-y^2}$-derived states in the valence band, only the basal oxygen ions are involved. In stark contrast, the Ni-$3d_{z^2}$-derived states in the valence and conduction band show a strong hybridization with the apical oxygen ions, but simultaneously minor contributions from the basal oxygen ions. Notably, the charge density at the inner apical oxygen site is considerably higher for the final than for the initial states; therefore, even an excitation with out-of-plane polarization is associated with a certain degree of charge transfer. This is consistent with the band structure [Fig. 1(f)], which uncovers an increasing involvement of oxygen in the Ni e_g states with increasing energy.

A further interesting unknown at the present time is the role of oxygen vacancies (V_O's) in the physics of bilayer nickelates [28, 31, 38]. It has been reported that the normal-state properties of $La_3Ni_2O_7$ depend sensitively on the oxygen content; in particular, oxygen appears to control the metallicity of the samples [44–46]. In order to obtain a first-principles impression of the trends in the optical spectrum, we consider an explicit single V_O in the unit cell. Surprisingly, we identify inner apical oxygen [site 3; see Fig. 1(d)] as the lowest formation energy site ($E_f^{V_O} = 2.99$ eV/V_O), which has been confirmed independently by high-resolution electron ptychography [47]. Still, this formation energy is higher than e.g. in perovskite $LaNiO_3$ (~ 2.8 eV [48]). The formation energies of basal V_O's (site 2, 3.53 eV/V_O) and outer apical V_O's (site 1, 5.06 eV/V_O) are even further enhanced and reach values reminiscent of $SrTiO_3$ [49, 50], which suppresses these defects exponentially.

Figure 1(a) shows that the presence of an explicit V_O leaves the overall structure of the in-plane optical spectrum invariant, but enhances the spectral weight below 0.6 eV and reduces the intensity of the two main peaks B and C, rendering values closer to experiment. Furthermore, the right slope of peak C becomes less steep and the spectral weight beyond $\omega > 2.6$ eV is increased, which also brings the simulated curve closer to experiment. Simultaneously, peak D can no longer be resolved, which indicates that the present V_O concentration (corresponding formally to $La_3Ni_2O_{6.75}$) is higher than in the experimental sample. For out-of-plane polarization [Fig. 1(b)], the intensity of peak B is significantly reduced, while peaks C and D are broadened and shifted to higher energies.

Inspection of Fig. 1(g) shows that the overall band structure and the TDMs stay similar to the stoichiometric case, particularly in the ideal bilayer without V_O. Interestingly, two defect states with strong Ni $3d_{z^2}$ character emerge at -0.8 and -1.5 eV. One of these states is split off from the conduction band and accommodates the two released electrons. Slight variations of E_F can be attributed to states with Ni $3d_{x^2-y^2}$ character around the M point, which experience a lifting of the degeneracy along the Brillouin zone boundary in the defective bilayer. Concomitantly, the Fermi surfaces show a strongly reconstructed shape and reduced Fermi velocity (i.e., increased resistivity; blue colors) in the defective bilayer, particularly near the M point [Fig. 1(g)].

This mechanism confines the impact of V_O's largely to the defective bilayers, while the remaining system shows an electronic structure close to the stoichiometric compound at only modest electron doping. This is reflected in the renormalizations of the optical spectrum, which we find to be moderate in view of the rather high V_O concentration considered here. We therefore speculate that the general nesting properties of the stoichiometric compound are relatively robust and may carry over to the Fermi surface in slightly oxygen-deficient samples, resulting in a similar superconducting pairing.

B. Correlation dependence of the optical spectrum

Next, we investigate how the ambient-pressure optical spectrum of $La_3Ni_2O_7$ varies with the Coulomb repulsion parameter, and estimate the strength of the electronic correlations in this system by comparison to recent experimental data.

Figure 2(a) shows that U has a very strong impact on the in-plane optical conductivity, affecting both its intensity and shape. Specifically, we observe a reduction in overall intensity from $U = 0$ to 5 eV, probably due to decreasing TDMs, and a simultaneously raising energy of peak C due to an increasing separation of the Ni $3d_{z^2}$ and Ni $3d_{x^2-y^2}$ states (see Supplementary Information). For higher U values, the energy of peak B is concomitantly decreased.

We identify the best overall agreement with recent experimental data [30] for $U = 3$ eV [Fig. 2(a)]. While the B-C energy difference is even more accurately described for yet smaller U values, the peak intensities are up to twice as high as the experimental curve, whereas the spectral weight for photon energies between $\omega \sim$ 2-3 eV is considerably underestimated. Good quantitative agreement is also found for $U = 4$ eV, albeit with overestimated B-C energy difference. For $U \geq 5$ eV, we find a clear disagreement with experiment that particularly manifests in the strongly overestimated B-C

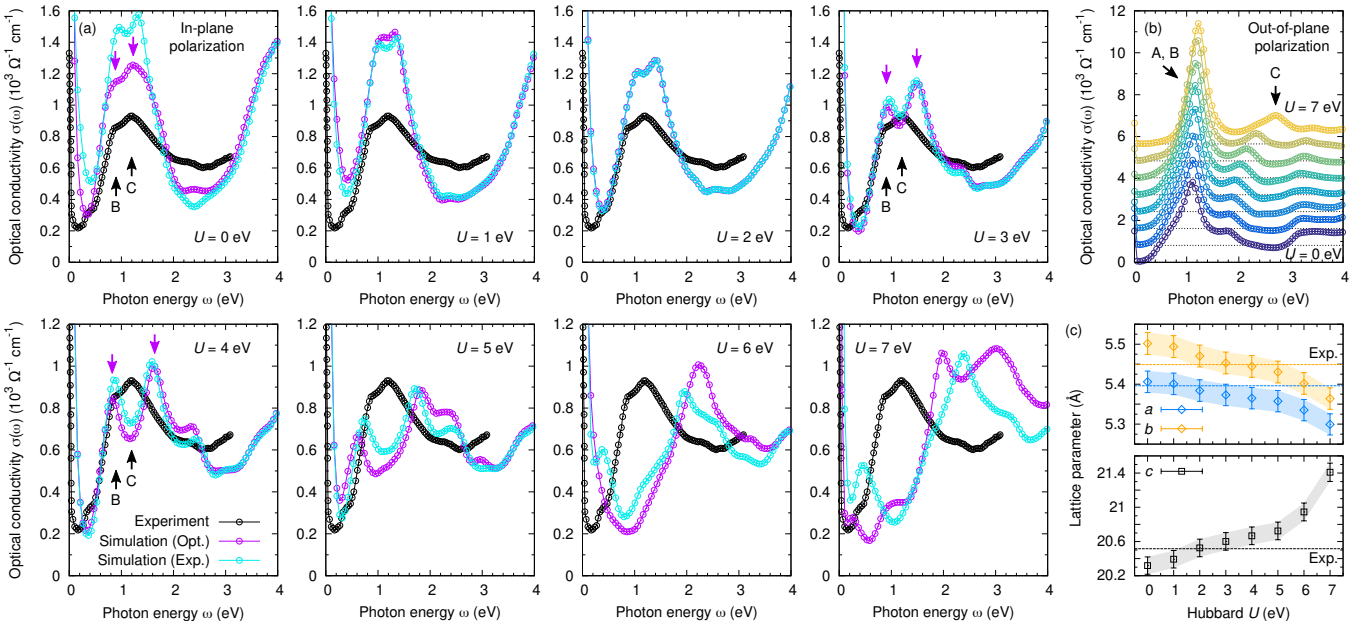

Figure 2. **Correlation dependence of the optical spectrum of $La_3Ni_2O_7$ at ambient pressure.** (a) Optical in-plane conductivity $\sigma_{xx,yy}(\omega)$ as a function of the on-site Coulomb repulsion parameter, exhibiting strong variations with U and very good quantitative agreement with experimental data (black [30]) around $U \sim 3$ eV. In addition to spectra obtained for consistently optimized lattice parameters (magenta), the panels show results for the experimental cell geometry (cyan). (b) Evolution of the corresponding out-of-plane component $\sigma_{zz}(\omega)$. (c) Optimized lattice parameters ($\pm 0.5\%$ error bar) compared to x-ray diffraction data [46], demonstrating very good agreement for $U \sim 1.5$-3.5 eV.

energy difference. This poses an upper limit to the static correlation effects in $La_3Ni_2O_7$.

Additionally, Fig. 2(b) displays the correlation dependence of the out-of-plane component $\sigma_{zz}(\omega)$. The characteristic peak around ~ 1.1 eV exhibits only a minor energy shift and predominantly becomes narrower with increasing U. In sharp contrast, peak C follows a pronounced nonlinear trajectory towards higher energies with increasing U, reflecting the continuous lowering of the occupied Ni $3d_{z^2}$ states and the concomitant raise of the Ni $3d_{x^2-y^2}$ states, particularly the empty ones around the M point (see Supplementary Information). At present, we are not aware of available experimental data for the out-of-plane component of the optical conductivity. Future measurements, particularly for peak C, would provide intriguing additional information about the correlation effects.

The quality of the estimated U value can be tested by analyzing the predicted cell geometry. Figure 2(c) shows that the in-plane lattice parameters a, b decrease monotonically from 5.41, 5.50 Å ($U = 0$ eV) to 5.30, 5.36 Å (7 eV). In sharp contrast, the out-of-plane lattice parameter c increases simultaneously from 20.32 to 21.41 Å. Consistent with the analysis of the optical spectrum, we find that $U \sim 1.5$-3.5 eV renders close agreement (within $\pm 0.5\%$ error bars) with the experimental lattice parameters $a = 5.396$, $b = 5.449$, $c = 20.516$ Å from x-ray diffraction (XRD) [31, 46].

Moreover, recent angle-resolved photoemission spectroscopy (ARPES) on $La_3Ni_2O_7$ identified the formation of Ni-$3d_{z^2}$-derived states ~ 50 meV below the Fermi level [34]. For $U = 3$ eV (4 eV), we observe the Ni $3d_{z^2}$ states ~ 60 meV (150 meV) below the Fermi energy (see Supplementary Information), an important agreement given current debates about the electronic structure of bilayer nickelates. This corroborates our conclusion in favor of $U \sim 3$ eV.

By comparing the Drude weight obtained from experiments to DFT calculations, previous work found that $La_3Ni_2O_7$ features strong electronic correlations that significantly reduce the kinetic energy of the electrons and place the bilayer nickelate in terms of Mottness close to the parent compound of cuprate superconductors La_2CuO_4 [30]. The present quantitative analysis of the optical *interband* transitions, which reflect the relative energies of the active Ni e_g orbitals and their distance to the O $2p$ states in the valence band, as well as the consistency with ARPES and XRD rather establish the notion of moderate electronic correlations in this novel high-T_c superconductor.

The rare-earth nickelates [51] including the infinite-layer compounds [52–55] are known to exhibit a more covalent nature and distinct Ni-O hybridization than related cuprates. Consequently, the latter are often described by higher Hubbard-U values such as 6.5 eV [56, 57] than nickelate systems (1-4 eV [58–64]). It has been reported that the bilayer nickelates show a strong involvement of the oxygen system as well [23, 31]. The resulting more delocalized wave functions rationalize the trend of reduced electronic correlations relative to the paradigmatic cuprate superconductors.

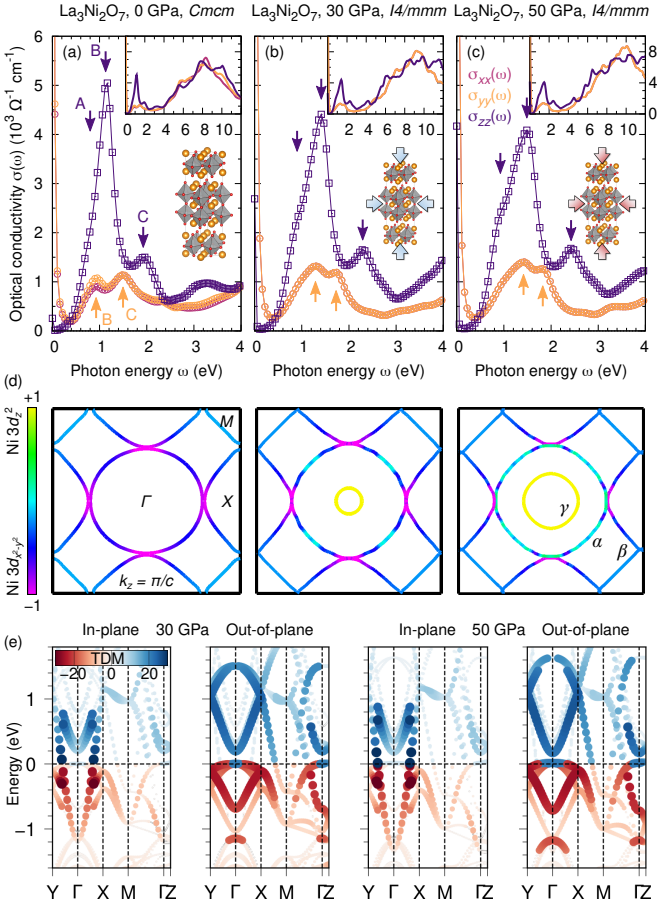

Figure 3. **Evolution of the optical spectrum of $La_3Ni_2O_7$ under high pressure.** Optical conductivities $\sigma_{xx}(\omega)$, $\sigma_{yy}(\omega)$, and $\sigma_{zz}(\omega)$ of $La_3Ni_2O_7$ (a) at ambient pressure, (b) at 30 GPa, and (c) at 50 GPa. The insets show a larger energy range. (d) Corresponding Fermi surfaces, colored by the Ni orbital character $(d_{z^2} - d_{x^2-y^2})/(d_{z^2} + d_{x^2-y^2})$. (e) Energy- and k-resolved transition dipole moments at 30 and 50 GPa (cf. Fig. 1) provide a microscopic explanation for the changes observed in the optical spectrum.

C. Evolution of the optical spectrum under high pressure

Based on these insights, we now predict the pressure dependence of the optical conductivity of $La_3Ni_2O_7$ consistently at $U = 3$ eV and thereby track the changes in the electronic structure across the structural phase transition.

Figure 3(a) shows $\sigma_{xx}(\omega)$, $\sigma_{yy}(\omega)$, and $\sigma_{zz}(\omega)$ for the orthorhombic $Cmcm$ geometry at ambient pressure. In sharp contrast to the pronounced in-plane versus out-of-plane anisotropy, the in-plane anisotropy $\sigma_{xx}(\omega) \neq \sigma_{yy}(\omega)$ is rather small. The inset shows that the optical spectrum exhibits a distinct 'hump' of moderate anisotropy between ~ 4 and 12 eV. We assign it predominantly to transitions from O $2p$ (below -2 eV) to La $5d$ (above 1.8 eV) [Fig. 1(f)]. Since the corresponding TDMs are relatively low, its considerable magnitude is a cumulative effect related to a high density of states.

At 30 GPa [Fig. 3(b)], the in-plane anisotropy vanishes due to the orthorhombic-to-tetragonal phase transition. The in-plane peaks B (1.3), C (1.7), and D (2.45 eV) as well as the out-of-plane peaks A (0.9), B (1.4), and C (2.3 eV) are shifted to higher photon energies. This can be understood from a pressure-enhanced energy difference between the lower and upper Ni $3d_{z^2}$ states that is accompanied by an increased energy of the Ni $3d_{x^2-y^2}$ states, specifically around the M point [31]. The in-plane peak A vanishes for finite pressure (not visible) due to the quenched octahedral rotations. Simultaneously, the Drude peak is considerably intensified due to the metallization of the Ni $3d_{z^2}$ states [γ pocket, Fig. 3(d)]: The DFT+U plasma frequencies increase from $\omega^2_{p,xx,yy} \sim 9.75$ to 16.65 eV^2 and from $\omega^2_{p,zz} \sim 0.02$ to 0.20 eV^2 (see Supplementary Information). The hump experiences a substantial broadening and now extends towards higher energies owing to the pressure-induced increase of the O $2p$ band width (lowering of the energy onset of the O $2p$ states) in the valence band [31].

At 50 GPa [Fig. 3(c)], the in-plane peaks B (1.4), C (1.8), and D (2.7 eV) as well as the out-of-plane peaks A (0.95), B (1.45), and C (2.4 eV) are shifted to even higher energies. Concomitantly, the out-of-plane Drude weight is further increased ($\omega^2_{p,zz} \sim 0.31$ eV^2).

Interestingly, we observe a pressure-induced intensity reduction of the out-of-plane peak B, which directly reflects the partial depletion of the 'bonding' Ni $3d_{z^2}$ states in the valence band [Figs. 3(e) and 1(f)]. Simultaneously, a new transition from ~ -1.2 eV to these depleted states becomes active [Fig. 3(e)]. Together with the Drude peak enhancement, this allows us to experimentally track the proposed emergence of a hole pocket γ [1, 11–14, 23, 28]), which plays a key role in the suggested $s^{\pm}$ superconductivity mechanism [12, 13, 22, 23, 28]. Therefore, the results promote optical spectroscopy as powerful technique to track transitions of the Fermi surface topology in high-pressure experiments.

D. Optical signature of different magnetic phases

Recent measurements suggested the presence of a spin-density wave (SDW) in $La_3Ni_2O_7$ at ambient pressure [38, 65]. However, nuclear diffraction and nuclear magnetic resonance studies found no long-range magnetic order [66, 67]. Motivated by this topical discussion, we explore the optical spectra for different magnetic phases in Fig. 4, which have been obtained by performing simulations for large supercells. We find a unique optical signature with strong in-plane versus out-of-plane anisotropy for each magnetic phase. For instance, the prominent peak in $\sigma_{zz}(\omega)$ (A, B) is shifted to higher energies (2.6-2.8 eV) for the $(\pi, 0)$ antiferromagnetic (AFM) stripe order suggested in Ref. [23] and the AFM-A order (with and without site disproportionation, i.e., an in-plane checkerboard charge and spin modulation [31]) and is less pronounced than in the nonmagnetic case. For all AFM phases [Fig. 4(c)-(f)], the $\sigma_{zz}(\omega)$ Drude peak is negligible or fully quenched, and the interband onset of $\sigma_{zz}(\omega)$ is found at higher energies than for $\sigma_{xx,yy}(\omega)$.

The $(\pi/2, \pi/2)$ bi-stripe AFM order superimposed by Ni^{2+}/Ni^{3+} charge order [Fig. 4(f)] has been proposed recently

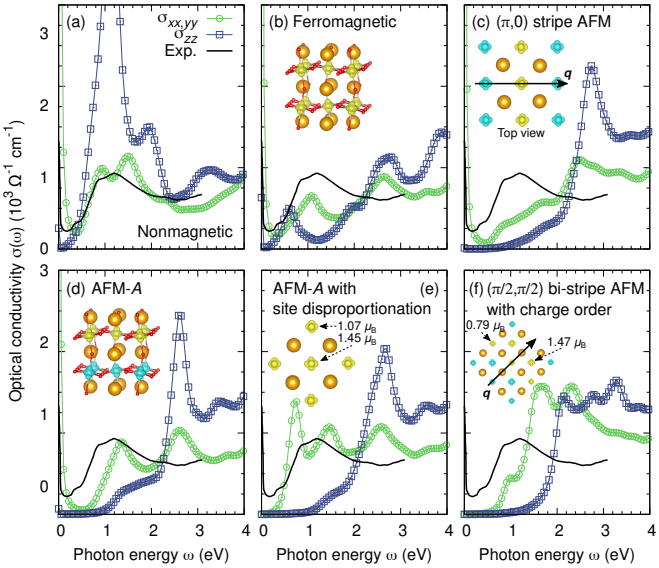

Figure 4. **Optical signature of different magnetic phases in $La_3Ni_2O_7$ at ambient pressure.** Compared are $\sigma_{xx,yy}(\omega)$ and $\sigma_{zz}(\omega)$ for (a) the nonmagnetic phase, (b) ferromagnetic order, (c) $(\pi, 0)$ antiferromagnetic (AFM) stripe order, (d) AFM-A order, (e) AFM-A order with in-plane site disproportionation, and (f) $(\pi/2, \pi/2)$ AFM charge-spin bi-stripe order as recently suggested SDW model. The structural models show the spin densities (yellow: positive; blue: negative). The interlayer coupling is AFM for (c)-(f), and only a single layer is shown in top view for (c),(e),(f). The experimental in-plane spectrum obtained at $T \sim 150$ K is displayed as black solid line [30].

by experiment [68] and theory [69] as good representation of the SDW in $La_3Ni_2O_7$. Similar to AFM-A order with site disproportionation, the $\sigma_{xx,yy}(\omega)$ Drude peak is absent due to the emergence of a finite band gap.

Interestingly, the experimental curve, which has been measured at $T \sim 150$ K [30] above the SDW transition, agrees best with the result of our nonmagnetic simulation, judging from the overall shape and peak positions of the interband spectrum together with the presence of a Drude peak. Notably, the sample remains metallic down to low temperatures [30]. These results will be helpful in the interpretation of future low-temperature studies.

E. Role of the layer stacking and comparison with related Ruddlesden-Popper nickelates

Finally, we discuss the results for the bilayer compound $La_3Ni_2O_7$ [Fig. 5(c)] in the broader context of related Ruddlesden-Popper (RP, $A_{n+1}Ni_nO_{3n+1}$) and reduced Ruddlesden-Popper (RRP, $A_{n+1}Ni_nO_{2n+2}$) nickelates.

We observe comparable shapes of the optical conductivity for the three RP members [Fig. 5(a-c)] shown. The trilayer nickelate $La_4Ni_3O_{10}$ [$n = 3$, Fig. 5(a)] has recently been proposed to be superconducting [71, 72]. The characteristic out-of-plane peak, which is found to universally stem from transitions between Ni-$3d_{z^2}$-derived quantum-well states [cf. Fig. 1(f)], is lowered to $\omega \sim 0.75$ eV due to the reduced quantum confinement relative to the bilayer compound.

An interesting variant of the $n = 2$ bilayer geometry is the recently observed 1-3 stacking [42, 43] [Fig. 5(b)]. We find it to be metastable and 82 meV/f.u. above the 2-2 ground state. The simulated spectra strongly resemble their $n = 3$ analogs. In particular, the characteristic out-of-plane peak appears at the same energy as in $La_4Ni_3O_{10}$, yet with reduced intensity. Unique manifestations of the single-layer $\sim 2+$ Ni states in the spectrum are not observed.

We find the best agreement of the experimental spectrum with our theoretical results for $La_3Ni_2O_7$ in the bilayer 2-2 stacking [Fig. 5(c)]. In contrast, in the predicted spectrum for the 1-3 stacking, the in-plane peak B is significantly lower than the experimental data and peak D is not visible at all, whereas peak C and the spectral weight below 0.6 eV are overestimated. We speculate that 2-2 and 1-3 phases may coexist in experimental samples. Intriguingly, the results establish $\sigma_{zz}(\omega)$ as ideal observable to quantify their relative volume fraction due to the highly characteristic peak energies.

Complete reduction of the apical oxygen in $La_3Ni_2O_7$ results in the RRP structure $La_3Ni_2O_6$ [73, 74] [Fig. 5(d)]. The formal Ni valence jumps from $2.5+$ to $1.5+$ due to the released electrons, which we find to be largely accommodated by the Ni $3d_{z^2}$ states. Hence, the spectral weight up to $\omega \sim 2$ eV is strongly suppressed; specifically, the characteristic peaks in $\sigma_{xx,yy}(\omega)$ and $\sigma_{zz}(\omega)$ vanish. A double peak appears in $\sigma_{zz}(\omega)$ between 2-3 eV, which is far less intense than in the RP nickelates and of different origin; we attribute it to transitions between Ni $3d_{z^2}$ and La $5d$ states.

The $n = \infty$ end member of the RRP series is the infinite-layer geometry [Fig. 5(e)], in which the Ni $3d_{z^2}$ states are fully occupied [53, 75]. Here we consider $NdNiO_2$ [Fig. 5(e)], which hosts superconductivity in film geometry [4]. The in-plane optical conductivity agrees reasonably with earlier DFT+DMFT simulations for $LaNiO_2$ [70] (inset), particular in the interband regime, which corroborates the validity of our approach. In addition, we predict the out-of-plane component, which uncovers a further reduced anisotropy. With respect to $La_3Ni_2O_6$, the interband onset of $\sigma_{zz}(\omega)$ shifts to lower energies and now coincides with $\sigma_{xx,yy}(\omega)$ at ~ 1 eV. While the characteristic peaks are absent, we find the higher-energy spectral weight to be enhanced in the RRP versus RP compounds.

These observations mirror fundamental differences in the electronic structure between the two Ruddlesden-Popper families. The successive occupation of the Ni $3d_{z^2}$ states provides each material with its unique optical signature. This manifests predominantly in the out-of-plane component, but also for in-plane polarization due to the pronounced Ni $3d_{x^2-y^2}$-$3d_{z^2}$ coupling (cf. Fig. 1). The optical spectra of the RP nickelates exhibit characteristic peaks with substantial anisotropy. In sharp contrast, since the Ni $3d_{z^2}$ states are largely filled in the RRP compounds, the corresponding spectra are dominated by the hump, which is complemented by excitations from Ni $3d$ to rare-earth $5d$ states and extends to lower energies due to the higher Fermi level.

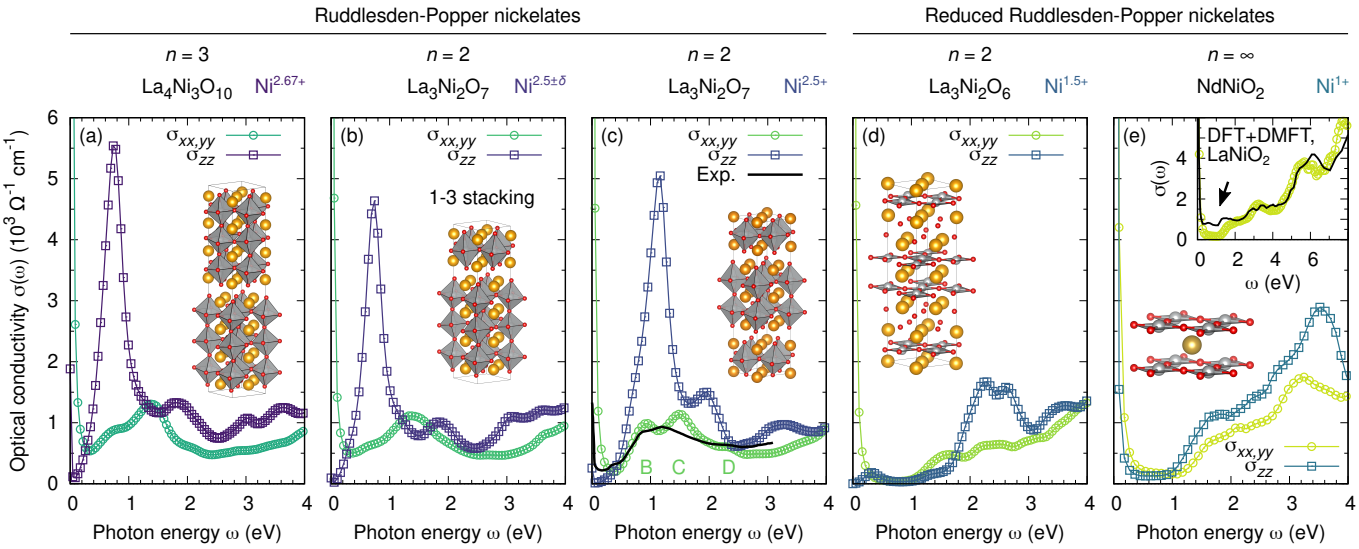

Figure 5. **Role of the layer stacking in $La_3Ni_2O_7$ and comparison with related Ruddlesden-Popper nickelates.** Optical conductivity (in-plane and out-of-plane) for different members of the Ruddlesden-Popper versus reduced Ruddlesden-Popper nickelates at ambient pressure, ordered by formal Ni valence (indicated by the color palette): (a) The $n = 3$ trilayer nickelate, (b) the $n = 2$ nickelate with 1-3 stacking, (c) the $n = 2$ bilayer nickelate (experimental spectrum from Ref. [30], black solid line), (d) the $n = 2$ reduced bilayer nickelate, and (e) the $n = \infty$ infinite-layer nickelate (in-plane DFT+DMFT spectrum from Ref. [70], black solid line in the inset).

III. DISCUSSION

The optical properties of $La_3Ni_2O_7$ bilayer nickelates were investigated by performing density functional theory simulations including a Coulomb repulsion term. We analyzed specifically the microscopic origin of the interband transitions, which reflect the relative energies of the active Ni e_g orbitals and their distance to the O $2p$ states in the valence band, and uncovered a surprisingly strong anisotropy of the optical response that reverses with frequency. The optical spectrum was found to be considerably impacted by on-site correlation effects, and very good agreement with experiment at ambient pressure is attained for $U \sim 3$ eV. This value simultaneously provides Ni $3d_{z^2}$ energies consistent with recent angle-resolved photoemission spectroscopy as well as lattice parameters that are in close agreement with x-ray diffraction.

The renormalizations of the optical spectrum due to oxygen vacancies, which were found to predominantly occur at the inner apical sites, further improve the agreement with experiment. Their explicit treatment revealed that the released electrons are largely accommodated by an emergent defect state, as opposed to charge doping the sample.

We found that the structural transition occurring under high pressure is accompanied by a significant enhancement of the Drude weight and a concomitant reduction of the out-of-plane interband component, which act as a fingerprint of the proposed Ni $3d_{z^2}$ hole pocket formation. This promotes optical spectroscopy as powerful technique to track transitions of the Fermi surface topology in high-pressure experiments.

Moreover, we identified the unique optical signature of different magnetic phases in $La_3Ni_2O_7$ at ambient pressure, including very recent models of spin-density waves. These insights will be helpful in the interpretation of future low-temperature studies.

Furthermore, we discussed the topical question of the 2-2 versus 1-3 layer stacking in $La_3Ni_2O_7$. The out-of-plane optical conductivity emerges as ideal observable to quantify the relative volume fraction of these possibly coexisting phases due to their highly characteristic peaks.

Finally, we broadened the perspective by comparing the bilayer nickelate to $La_4Ni_3O_{10}$, $La_3Ni_2O_6$, and $NdNiO_2$, which unveiled that each material exhibits its unique optical signature. We identified fundamental differences between Ruddlesden-Popper and reduced Ruddlesden-Popper nickelates, but also general trends that relate to the formal Ni valence.

In conclusion, the present comprehensive study establishes the notion of rather moderate electronic correlations in $La_3Ni_2O_7$. The uncovered trends and their microscopic analysis may guide future experiments, support the quest towards understanding the origin of superconductivity in this high-T_c nickelate, and accelerate the discovery of related compounds with enhanced properties.

METHODS

Density functional theory calculations

We performed first-principles simulations in the framework of (spin-polarized) density functional theory (DFT [76]) as implemented in the *Vienna Ab initio Simulation Package* (VASP) [77, 78], employing a wave-function cutoff of 520 eV. Exchange and correlations were described by using

the generalized gradient approximation as parameterized by Perdew, Burke, and Ernzerhof [79]. Static correlation effects were considered within the DFT+U formalism [80, 81], using $U = 3$ eV at the Ni sites unless stated otherwise.

To account for octahedral tilts and oxygen vacancies, the $La_3Ni_2O_{7-\delta}$ bilayer nickelates ($\delta = 0, 0.25$) were modeled by using orthorhombic 48-atom unit cells. The Brillouin zone was sampled employing $12 \times 12 \times 4$ Monkhorst-Pack [82] and Γ-centered $19 \times 19 \times 5$ $\vec{k}$-point grids in conjunction with a Gaussian smearing of 5 mRy. The lattice parameters a, b and c as well as the internal ionic positions were accurately optimized in DFT+U under zero and finite external pressure, reducing ionic forces below 1 mRy/a.u. We proceeded analogously for $La_4Ni_3O_{10}$, $La_3Ni_2O_6$, and $NdNiO_2$.

The oxygen vacancy formation energies are related to the DFT+U total energies via

$$E_f^{\mathrm{Vo}} = E(\mathrm{La_3Ni_2O_{7-\delta}}) - E(\mathrm{La_3Ni_2O_7}) + \delta\,\mu_{\mathrm{O}}\,, \qquad (1)$$

where $\mu_{\mathrm{O}} = \frac{1}{2}E(\mathrm{O_2})$ models the oxygen-rich limit. The well-known overbinding of gas-phase O_2 molecules in DFT necessitates a correction of $E(O_2)$, which we performed such as to reproduce the experimental O_2 binding energy of 5.16 eV [48, 50, 83–86].

We obtain the imaginary part of the frequency-dependent dielectric function $\varepsilon_{\alpha\beta}(\omega) = \varepsilon^{(1)}_{\alpha\beta}(\omega) + i\,\varepsilon^{(2)}_{\alpha\beta}(\omega)$ from the cell-periodic parts of the Kohn-Sham states $|n, \vec{k}\rangle$ and the corresponding eigenenergies $\epsilon_{n,\vec{k}}$ by evaluating [87]

$$\varepsilon^{(2)}_{\alpha\beta}(\omega) = \frac{4\pi^2 e^2}{\Omega} \lim_{q\to 0} \frac{1}{q^2} \sum_{c,v,\vec{k}} 2w_{\vec{k}}\,\delta(\epsilon_{c,\vec{k}} - \epsilon_{v,\vec{k}} - \omega) \times \langle c, \vec{k} + q\vec{e}_\alpha | v, \vec{k}\rangle \langle v, \vec{k} | c, \vec{k} + q\vec{e}_\beta\rangle. \qquad (2)$$

Here, $\alpha, \beta \in \{x, y, z\}$ label the different spatial directions, Ω denotes the unit cell volume, and c and v enumerate the conduction and valence band states, respectively. These interband contributions are complemented by the Drude peak:

$$\varepsilon^{(2)}_{\alpha\beta}(\omega) = \frac{\Gamma}{\omega}\frac{\omega^2_{p,\alpha\beta}}{\omega^2 + \Gamma^2}. \qquad (3)$$

We predict the plasma frequency squared $\omega^2_{p,\alpha\beta}$ directly from the DFT+U electronic structure (see Supplementary Information). In contrast, the lifetime Γ is considerably more difficult to obtain. We employ $\Gamma = 10$ meV here, motivated by recent experimental Drude peak analysis for $La_3Ni_2O_7$ [30] and DFT+DMFT results for $LaNiO_2$ [70]. Subsequently, the real part of the optical conductivity is obtained via

$$\sigma_{\alpha\beta}(\omega) = \varepsilon_0\,\omega\,\varepsilon^{(2)}_{\alpha\beta}(\omega) \qquad (4)$$

$$\sigma_{xx,yy}(\omega) = \frac{\sigma_{xx}(\omega) + \sigma_{yy}(\omega)}{2}. \qquad (5)$$

To disentangle the individual contributions to the optical spectrum, we calculate the transition dipole moments (TDMs),

$$\vec{P}(n, \vec{k} \to n', \vec{k}') = \langle n', \vec{k}' | e\hat{\vec{r}} | n, \vec{k}\rangle = \frac{i\hbar e}{(\epsilon_{n,\vec{k}} - \epsilon_{n',\vec{k}'})\,m} \langle n', \vec{k}' | \hat{\vec{p}} | n, \vec{k}\rangle \qquad (6)$$

which determine how the system interacts with an electromagnetic wave of a given polarization. The sum of squares P^2 is the transition probability between two states. To visualize the TDMs in a compact, yet energy- and k-resolved form, we construct the following cumulative quantities for each valence and conduction band state from the squares of the distinct vector components:

$$P^2_\alpha(v, \vec{k}) = \sum_c P^2_\alpha(v, \vec{k} \to c, \vec{k}), \qquad (7)$$

$$P^2_\alpha(c, \vec{k}) = \sum_v P^2_\alpha(v, \vec{k} \to c, \vec{k}). \qquad (8)$$

DATA AVAILABILITY

The data is available upon reasonable request to the authors.

ACKNOWLEDGMENTS

We thank Prof. Roser Valentí for helpful discussions. This work was supported by the National Science Foundation, Grant No. NSF-DMR-2118718. L. F. acknowledges support by the European Union's Horizon 2020 research and innovation programme through the Marie Skłodowska-Curie grant SuperCoop (Grant No. 838526).

AUTHOR CONTRIBUTIONS

BG, LF, and PJH conceived of the project. JJH, GRS, RGH, and PJH supervised the research. BG performed the theoretical simulations and corresponding analysis. BG, LF, and PJH wrote the paper. All authors discussed the results and revised the paper.

COMPETING INTERESTS

The authors declare no competing interests.

[1] Sun, H. *et al.* Signatures of superconductivity near 80 K in a nickelate under high pressure. *Nature* **621**, 493–498 (2023).

[2] Hou, J. *et al.* Emergence of high-temperature superconducting phase in pressurized $La_3Ni_2O_7$ crystals. *Chin. Phys. Lett.* **40**,

117302 (2023).

[3] Zhang, Y. *et al.* High-temperature superconductivity with zero-resistance and strange metal behavior in $La_3Ni_2O_7$. Preprint at https://arxiv.org/abs/2307.14819 (2023).

[4] Li, D. *et al.* Superconductivity in an infinite-layer nickelate. *Nature* **572**, 624–627 (2019).

[5] Li, D. *et al.* Superconducting dome in $Nd_{1-x}Sr_xNiO_2$ infinite layer films. *Phys. Rev. Lett.* **125**, 027001 (2020).

[6] Zeng, S. *et al.* Phase diagram and superconducting dome of infinite-layer $Nd_{1-x}Sr_xNiO_2$ thin films. *Phys. Rev. Lett.* **125**, 147003 (2020).

[7] Osada, M. *et al.* A superconducting praseodymium nickelate with infinite layer structure. *Nano Lett.* **20**, 5735–5740 (2020).

[8] Osada, M. *et al.* Nickelate superconductivity without rare-earth magnetism: (La,Sr)NiO_2. *Adv. Mater.* **33**, 2104083 (2021).

[9] Pan, G. A. *et al.* Superconductivity in a quintuple-layer square-planar nickelate. *Nat. Mater.* **21**, 160–164 (2022).

[10] Goodge, B. H. *et al.* Resolving the polar interface of infinite-layer nickelate thin films. *Nat. Mater.* **22**, 466–473 (2023).

[11] Luo, Z., Hu, X., Wang, M., Wú, W. & Yao, D.-X. Bilayer two-orbital model of $La_3Ni_2O_7$ under pressure. *Phys. Rev. Lett.* **131**, 126001 (2023).

[12] Gu, Y., Le, C., Yang, Z., Wu, X. & Hu, J. Effective model and pairing tendency in bilayer Ni-based superconductor $La_3Ni_2O_7$. Preprint at https://arxiv.org/abs/2306.07275 (2023).

[13] Yang, Q.-G., Wang, D. & Wang, Q.-H. Possible $s_{\pm}$-wave superconductivity in $La_3Ni_2O_7$. *Phys. Rev. B* **108**, L140505 (2023).

[14] Lechermann, F., Gondolf, J., Bötzel, S. & Eremin, I. M. Electronic correlations and superconducting instability in $La_3Ni_2O_7$ under high pressure. *Phys. Rev. B* **108**, L201121 (2023).

[15] Sakakibara, H., Kitamine, N., Ochi, M. & Kuroki, K. Possible high T_c superconductivity in $La_3Ni_2O_7$ under high pressure through manifestation of a nearly half-filled bilayer Hubbard model. *Phys. Rev. Lett.* **132**, 106002 (2024).

[16] Shen, Y., Qin, M. & Zhang, G.-M. Effective bi-layer model hamiltonian and density-matrix renormalization group study for the high-T_c superconductivity in $La_3Ni_2O_7$ under high pressure. *Chin. Phys. Lett.* **40**, 127401 (2023).

[17] Christiansson, V., Petocchi, F. & Werner, P. Correlated electronic structure of $La_3Ni_2O_7$ under pressure. *Phys. Rev. Lett.* **131**, 206501 (2023).

[18] Shilenko, D. A. & Leonov, I. V. Correlated electronic structure, orbital-selective behavior, and magnetic correlations in double-layer $La_3Ni_2O_7$ under pressure. *Phys. Rev. B* **108**, 125105 (2023).

[19] Wú, W., Luo, Z., Yao, D.-X. & Wang, M. Superexchange and charge transfer in the nickelate superconductor $La_3Ni_2O_7$ under pressure. *Science China Physics, Mechanics & Astronomy* **67**, 117402 (2024).

[20] Cao, Y. & Yang, Y.-f. Flat bands promoted by Hund's rule coupling in the candidate double-layer high-temperature superconductor $La_3Ni_2O_7$ under high pressure. *Phys. Rev. B* **109**, L081105 (2024).

[21] Chen, X., Jiang, P., Li, J., Zhong, Z. & Lu, Y. Critical charge and spin instabilities in superconducting $La_3Ni_2O_7$. Preprint at https://arxiv.org/abs/2307.07154 (2023).

[22] Lu, C., Pan, Z., Yang, F. & Wu, C. Interlayer coupling driven high-temperature superconductivity in $La_3Ni_2O_7$ under pressure. Preprint at https://arxiv.org/abs/2307.14965 (2023).

[23] Zhang, Y., Lin, L.-F., Moreo, A., Maier, T. A. & Dagotto, E. Structural phase transition, s±-wave pairing, and magnetic stripe order in bilayered superconductor $La_3Ni_2O_7$ under pressure. *Nat. Commun.* **15**, 2470 (2024).

[24] Liao, Z. *et al.* Electron correlations and superconductivity in $La_3Ni_2O_7$ under pressure tuning. Preprint at https://arxiv.org/abs/2307.16697 (2023).

[25] Qu, X.-Z. *et al.* Bilayer t-j-$j_{\perp}$ model and magnetically mediated pairing in the pressurized nickelate $La_3Ni_2O_7$. *Phys. Rev. Lett.* **132**, 036502 (2024).

[26] Huang, J., Wang, Z. D. & Zhou, T. Impurity and vortex states in the bilayer high-temperature superconductor $La_3Ni_2O_7$. *Phys. Rev. B* **108**, 174501 (2023).

[27] Qin, Q. & Yang, Y.-f. High-T_c superconductivity by mobilizing local spin singlets and possible route to higher T_c in pressurized $La_3Ni_2O_7$. *Phys. Rev. B* **108**, L140504 (2023).

[28] Liu, Y.-B., Mei, J.-W., Ye, F., Chen, W.-Q. & Yang, F. $s^{\pm}$-wave pairing and the destructive role of apical-oxygen deficiencies in $La_3Ni_2O_7$ under pressure. *Phys. Rev. Lett.* **131**, 236002 (2023).

[29] Zhang, Y., Lin, L.-F., Moreo, A., Maier, T. A. & Dagotto, E. Trends in electronic structures and $s_{\pm}$-wave pairing for the rare-earth series in bilayer nickelate superconductor $R_3Ni_2O_7$. *Phys. Rev. B* **108**, 165141 (2023).

[30] Liu, Z. *et al.* Electronic correlations and energy gap in the bilayer nickelate $La_3Ni_2O_7$. Preprint at https://arxiv.org/abs/2307.02950 (2023).

[31] Geisler, B., Hamlin, J. J., Stewart, G. R., Hennig, R. G. & Hirschfeld, P. J. Structural transitions, octahedral rotations, and electronic properties of $A_3Ni_2O_7$ rare-earth nickelates under high pressure. *npj Quantum Materials* **9**, 38 (2024).

[32] Rhodes, L. C. & Wahl, P. Structural routes to stabilise superconducting $La_3Ni_2O_7$ at ambient pressure. Preprint at https://arxiv.org/abs/2309.15745 (2023).

[33] Wang, G. *et al.* Pressure-induced superconductivity in polycrystalline $La_3Ni_2O_7$. Preprint at https://arxiv.org/abs/2309.17378 (2023).

[34] Yang, J. *et al.* Orbital-dependent electron correlation in double-layer nickelate $La_3Ni_2O_7$. Preprint at https://arxiv.org/abs/2309.01148 (2023).

[35] Lu, C., Pan, Z., Yang, F. & Wu, C. Interplay of two e_g orbitals in superconducting $La_3Ni_2O_7$ under pressure. Preprint at https://arxiv.org/abs/2310.02915 (2023).

[36] Wang, G. *et al.* Observation of high-temperature superconductivity in the high-pressure tetragonal phase of $La_2PrNi_2O_{7-\delta}$. Preprint at https://arxiv.org/abs/2311.08212 (2023).

[37] Wang, L. *et al.* Structure responsible for the superconducting state in $La_3Ni_2O_7$ at high pressure and low temperature conditions. Preprint at https://arxiv.org/abs/2311.09186 (2023).

[38] Chen, K. *et al.* Evidence of spin density waves in $La_3Ni_2O_{7-\delta}$. *Phys. Rev. Lett.* **132**, 256503 (2024).

[39] Zheng, Y.-Y. & Wu, W. Superconductivity in the bilayer two-orbital hubbard model. Preprint at https://arxiv.org/abs/2312.03605 (2023).

[40] Kakoi, M., Kaneko, T., Sakakibara, H., Ochi, M. & Kuroki, K. Pair correlations of the hybridized orbitals in a ladder model for the bilayer nickelate $La_3Ni_2O_7$. Preprint at https://arxiv.org/abs/2312.04304 (2023).

[41] Qazilbash, M. M. *et al.* Electronic correlations in the iron pnictides. *Nature Physics* **5**, 647–650 (2009).

[42] Chen, X. *et al.* Polymorphism in the ruddlesden–popper nickelate $La_3Ni_2O_7$: Discovery of a hidden phase with distinctive layer stacking. *Journal of the American Chemical Society* **146**, 3640–3645 (2024).

[43] Puphal, P. *et al.* Unconventional crystal structure of the high-pressure superconductor $La_3Ni_2O_7$. Preprint at https://arxiv.org/abs/2312.07341 (2023).

[44] Wu, G., Neumeier, J. J. & Hundley, M. F. Magnetic susceptibility, heat capacity, and pressure dependence of the electri-

cal resistivity of $La_3Ni_2O_7$ and $La_4Ni_3O_{10}$. *Phys. Rev. B* **63**, 245120 (2001).

[45] Taniguchi, S. *et al.* Transport, magnetic and thermal properties of $La_3Ni_2O_{7-\delta}$. *J. Phys. Soc. Jpn.* **64**, 1644–1650 (1995).

[46] Zhang, Z., Greenblatt, M. & Goodenough, J. Synthesis, structure, and properties of the layered perovskite $La_3Ni_2O_{7-\delta}$. *J. Solid State Chem.* **108**, 402–409 (1994).

[47] Dong, Z. *et al.* Visualization of oxygen vacancies and self-doped ligand holes in $La_3Ni_2O_{7-\delta}$. *Nature* **630**, 847–852 (2024).

[48] Malashevich, A. & Ismail-Beigi, S. First-principles study of oxygen-deficient $LaNiO_3$ structures. *Phys. Rev. B* **92**, 144102 (2015).

[49] Geisler, B. & Pentcheva, R. Fundamental difference in the electronic reconstruction of infinite-layer versus perovskite neodymium nickelate films on $SrTiO_3(001)$. *Phys. Rev. B* **102**, 020502(R) (2020).

[50] Sahinovic, A. & Geisler, B. Active learning and element-embedding approach in neural networks for infinite-layer versus perovskite oxides. *Phys. Rev. Research* **3**, L042022 (2021).

[51] Middey, S. *et al.* Physics of ultrathin films and heterostructures of rare-earth nickelates. *Annu. Rev. Mater. Res.* **46**, 305–334 (2016).

[52] Lee, K.-W. & Pickett, W. E. Infinite-layer $LaNiO_2$: Ni^{1+} is not Cu^{2+}. *Phys. Rev. B* **70**, 165109 (2004).

[53] Botana, A. S. & Norman, M. R. Similarities and differences between $LaNiO_2$ and $CaCuO_2$ and implications for superconductivity. *Phys. Rev. X* **10**, 011024 (2020).

[54] Geisler, B. & Pentcheva, R. Correlated interface electron gas in infinite-layer nickelate versus cuprate films on $SrTiO_3(001)$. *Phys. Rev. Research* **3**, 013261 (2021).

[55] Geisler, B. Rashba spin-orbit coupling in infinite-layer nickelate films on $SrTiO_3(001)$ and $KTaO_3(001)$. *Phys. Rev. B* **108**, 224502 (2023).

[56] Anisimov, V. I., Zaanen, J. & Andersen, O. K. Band theory and Mott insulators: Hubbard U instead of Stoner I. *Phys. Rev. B* **44**, 943 (1991).

[57] Zhong, Z., Koster, G. & Kelly, P. J. Prediction of thickness limits of ideal polar ultrathin films. *Phys. Rev. B* **85**, 121411 (2012).

[58] May, S. J. *et al.* Quantifying octahedral rotations in strained perovskite oxide films. *Phys. Rev. B* **82**, 014110 (2010).

[59] Chakhalian, J. *et al.* Asymmetric orbital-lattice interactions in ultrathin correlated oxide films. *Phys. Rev. Lett.* **107**, 116805 (2011).

[60] Gibert, M., Zubko, P., Scherwitzl, R., Íñiguez, J. & Triscone, J.-M. Exchange bias in $LaNiO_3$–$LaMnO_3$ superlattices. *Nat. Mater.* **11**, 195–198 (2012).

[61] Liu, J. *et al.* Heterointerface engineered electronic and magnetic phases of $NdNiO_3$ thin films. *Nat. Commun.* **4**, 2714 (2013).

[62] Kim, H.-S. & Han, M. J. Effect of charge doping on the electronic structure, orbital polarization, and structural distortion in nickelate superlattice. *Phys. Rev. B* **91**, 235102 (2015).

[63] Geisler, B., Blanca-Romero, A. & Pentcheva, R. Design of n- and p-type oxide thermoelectrics in $LaNiO_3/SrTiO_3(001)$ superlattices exploiting interface polarity. *Phys. Rev. B* **95**, 125301 (2017).

[64] Geisler, B. & Pentcheva, R. Confinement- and strain-induced enhancement of thermoelectric properties in $LaNiO_3/LaAlO_3(001)$ superlattices. *Phys. Rev. Materials* **2**, 055403 (2018).

[65] Liu, Z. *et al.* Evidence for charge and spin density waves in single crystals of $La_3Ni_2O_7$ and $La_3Ni_2O_6$. *Sci. China Phys. Mech. Astron.* **66**, 217411 (2022).

[66] Ling, C. D., Argyriou, D. N., Wu, G. & Neumeier, J. Neutron diffraction study of $La_3Ni_2O_7$: Structural relationships among n =1, 2, and 3 phases $La_{n+1}Ni_nO_{3n+1}$. *J. Solid State Chem.* **152**, 517–525 (2000).

[67] Fukamachi, T., Kobayashi, Y., Miyashita, T. & Sato, M. ^{139}La NMR studies of layered perovskite systems $La_3Ni_2O_{7-\delta}$ and $La_4Ni_3O_{10}$. *J. Phys. Chem. Solids* **62**, 195–198 (2001).

[68] Chen, X. *et al.* Electronic and magnetic excitations in $La_3Ni_2O_7$. URL https://arxiv.org/abs/2401.12657. Preprint at https://arxiv.org/abs/2401.12657 (2024).

[69] LaBollita, H., Pardo, V., Norman, M. R. & Botana, A. S. Assessing the formation of spin and charge stripes in $La_3Ni_2O_7$ from first-principles. URL https://arxiv.org/abs/2407.14409. Preprint at https://arxiv.org/abs/2407.14409 (2024).

[70] Kang, C.-J. & Kotliar, G. Optical properties of the infinite-layer $la_{1-x}sr_xnio_2$ and hidden hund's physics. *Phys. Rev. Lett.* **126**, 127401 (2021).

[71] Zhu, Y. *et al.* Superconductivity in trilayer nickelate $La_4Ni_3O_{10}$ single crystals. Preprint at https://arxiv.org/abs/2311.07353 (2024).

[72] Zhang, M. *et al.* Superconductivity in trilayer nickelate $La_4Ni_3O_{10}$ under pressure. Preprint at https://arxiv.org/abs/2311.07423 (2024).

[73] Pardo, V. & Pickett, W. E. Metal-insulator transition in layered nickelates $la_3ni_2o_{7-\delta}$ ($\delta = 0.0, 0.5, 1$). *Phys. Rev. B* **83**, 245128 (2011).

[74] Zhang, Y., Lin, L.-F., Moreo, A., Maier, T. A. & Dagotto, E. Electronic structure, magnetic correlations, and superconducting pairing in the reduced ruddlesden-popper bilayer $La_3Ni_2O_6$ under pressure: Different role of $d_{3z^2-r^2}$ orbital compared with $La_3Ni_2O_7$. *Phys. Rev. B* **109**, 045151 (2024).

[75] Sahinovic, A., Geisler, B. & Pentcheva, R. Nature of the magnetic coupling in infinite-layer nickelates versus cuprates. *Phys. Rev. Mater.* **7**, 114803 (2023).

[76] Kohn, W. & Sham, L. J. Self-consistent equations including exchange and correlation effects. *Phys. Rev.* **140**, A1133–A1138 (1965).

[77] Kresse, G. & Joubert, D. From ultrasoft pseudopotentials to the projector augmented-wave method. *Phys. Rev. B* **59**, 1758–1775 (1999).

[78] Blöchl, P. E. Projector augmented-wave method. *Phys. Rev. B* **50**, 17953–17979 (1994).

[79] Perdew, J. P., Burke, K. & Ernzerhof, M. Generalized gradient approximation made simple. *Phys. Rev. Lett.* **77**, 3865–3868 (1996).

[80] Liechtenstein, A. I., Anisimov, V. I. & Zaanen, J. Density-functional theory and strong interactions: Orbital ordering in Mott-Hubbard insulators. *Phys. Rev. B* **52**, R5467 (1995).

[81] Dudarev, S. L., Botton, G. A., Savrasov, S. Y., Humphreys, C. J. & Sutton, A. P. Electron-energy-loss spectra and the structural stability of nickel oxide: An LSDA+U study. *Phys. Rev. B* **57**, 1505 (1998).

[82] Monkhorst, H. J. & Pack, J. D. Special points for Brillouin-zone integrations. *Phys. Rev. B* **13**, 5188 (1976).

[83] Geisler, B. & Pentcheva, R. Inducing n- and p-type thermoelectricity in oxide superlattices by strain tuning of orbital-selective transport resonances. *Phys. Rev. Applied* **11**, 044047 (2019).

[84] Geisler, B. & Pentcheva, R. Competition of defect ordering and site disproportionation in strained $LaCoO_3$ on $SrTiO_3(001)$. *Phys. Rev. B* **101**, 165108 (2020).

[85] Sahinovic, A. & Geisler, B. Quantifying transfer learning synergies in infinite-layer and perovskite nitrides, oxides, and fluo-

rides. *J. Phys.: Condens. Matter* **34**, 214003 (2022).

[86] Geisler, B., Follmann, S. & Pentcheva, R. Oxygen vacancy formation and electronic reconstruction in strained $LaNiO_3$ and $LaNiO_3/LaAlO_3$ superlattices. *Phys. Rev. B* **106**, 155139 (2022).

[87] Gajdoš, M., Hummer, K., Kresse, G., Furthmüller, J. & Bechstedt, F. Linear optical properties in the projector-augmented wave methodology. *Phys. Rev. B* **73**, 045112 (2006).